ACS OMEGA

Open Access

http://pubs.acs.org/journal/acsodf

Article

Comparative Study of the Electrorheological Properties of Various Halide Perovskites

Suk Jekal,[⊥] Hyuntae Choi,[⊥] Zambaga Otgonbayar, Jiwon Kim, Yoon-Ho Ra, Jeongin Lim, Young Un Jeon, Jeoung Han Kim, Jinsung Rho, Seulki Song,* and Chang-Min Yoon*

Cite This: *ACS Omega* 2025, 10, 13327−13338

Read Online

ACCESS | Metrics & More | Article Recommendations | Supporting Information

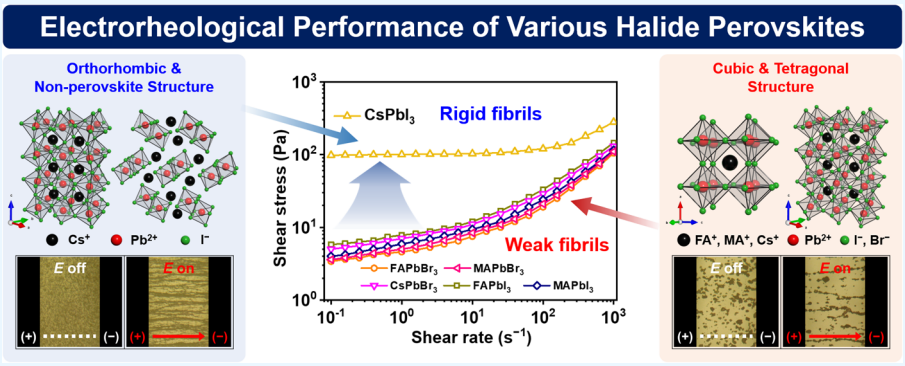

ABSTRACT: Although perovskite-structured materials have primarily been widely employed in solar cell applications, limited studies have been conducted in the field of electrorheology (ER). In this study, various halide perovskite materials, including $FAPbBr_3$, $FAPbI_3$, $MAPbBr_3$, $MAPbI_3$, $CsPbBr_3$, and $CsPbI_3$ were synthesized for the first time to evaluate their applicability in ER for the first time. Initially, the morphological and chemical properties of these materials were characterized to confirm the successful formation of the perovskite structures. In addition, the as-synthesized halide perovskite materials were dispersed in silicone oil (3.0 wt %) to evaluate their suitability as dispersants in ER fluids. Among these, the $CsPbI_3$-based ER fluid exhibited the optimal dielectric properties and the greatest dispersion stability of the various systems examined. In ER applications, the $CsPbI_3$-based ER fluid demonstrated the highest ER performance, achieving a shear stress of 99.4 Pa, owing to the synergistic effects of its intrinsic rod-like structure and dielectric properties, which promoted polarization. The aspect ratios of the $CsPbI_3$ rods were further controlled by modifying the synthetic process, resulting in the generation of both shorter and longer rods. Notably, ER fluids based on $CsPbI_3$ synthesized via a hydrothermal method yielded rod-like structures with a high aspect ratio of 20, leading to an enhanced ER activity of 128.0 Pa. These results highlight the potential of halide perovskite materials for use in ER applications.

INTRODUCTION

Electrorheological (ER) fluids consist of highly dielectric materials dispersed in nonconductive media, including silicone or mineral oil.[1] ER fluids have attracted considerable attention due to their ability to rapidly alter their viscosities and rheological properties under an electric (E) field.[2] More specifically, upon the application of an E field, the dispersed particles become polarized, aligning them into fibril-like structures along the direction of the field.[3] This arrangement allows the ER fluids to transition from a liquid-like state to a solid-like state, thereby gaining mechanical strength.[4] When the E field is removed, the ER fluids revert to their original liquid states.[5] Because of their reversible and fast response characteristics, ER fluids are suitable for use in various industrial applications, including haptic devices, clutch systems, dampers, and actuators.[6,7] The performances of ER fluids generally depend on the degree of polarization of the dispersed particles within the medium.[8] Strong polarization can be achieved by selecting dispersants with high dielectric constants.[9] To date, various polarizable materials such as inorganic, organic, metallic, and polymeric materials have been employed as dispersing materials.[10−13] Recently, perovskite materials have gained attention for use in ER applications owing to their high tunabilities, excellent dielectric properties, and desirable structural diversities.[14,15] Perovskites typically exhibit an ABX_3 structure, in which the A-site can be occupied by alkaline metals and organic cations, the B-site generally

Received: December 12, 2024
Revised: January 22, 2025
Accepted: March 18, 2025
Published: March 27, 2025

hosts transition metal ions, and the X-site is occupied by anions, including oxygen or halides.[16]

Perovskite materials exhibit distinct dielectric and optical properties depending on their phases, particularly among the alpha (α)-, beta (β)-, gamma (γ)-, and delta (δ)-phases, all of which are influenced by their composition and environmental conditions.[17] The α-phase, which is stable at higher temperatures (>300 °C), exhibits a more uniform and ionic arrangement in cubic structures, resulting in balanced optical and electronic properties that are advantageous for optoelectronic applications, such as solar cells.[18] It is known that the α-phase materials often display dark colors, such as black, due to their efficient light-absorbing properties. The β-phase, which is stable at lower temperatures compared to the α-phase, features a tetragonal structure with slightly distorted symmetry. The γ-phase adopts an orthorhombic structure with further reduced symmetry, typically forming at lower temperatures where the material exhibits high thermodynamic stability. Structural distortion and reduced symmetry in the γ-phase enhances the polarizability of the material, thereby improving its dielectric properties.[19] The δ-phase is a nonperovskite structure with a one-dimensional edge-sharing $[BX_6]^{4-}$ octahedral chain structure.[20] Unlike other phases, the δ-phase exhibits a large bandgap, resulting in reduced optical absorption and a yellowish color. Typically stable at room temperature, δ-phase materials exhibit enhanced polarizability, which is advantageous in the field of ER fluids by promoting stronger interactions with the applied E field.[21]

Although the polarizability of a material mainly depends on its type and dielectric properties, geometrical factors such as the size, morphology, shape, and porosity also significantly affect polarization. Previous studies have shown that elongated materials, including nanofibers, nanorods, and nanotubes, can have a positive effect on the ER performance because of their shape advantages.[22,23] An increased aspect ratio can enhance both the mechanical stability and the dielectric properties, leading to an enhanced ER activity compared with spherical or polyhedral materials.[24] In this context, Noh et al. reported differences in the ER performances of mesoporous silica materials coated by polyaniline with aspect ratios (L/D) of 1, 5, and 10, demonstrating that high aspect ratios resulted in higher ER activities.[25] Although several studies have emphasized the ER effects of materials with various aspect ratios, few have reported a direct correlation between the aspect ratio of a material and its ER performance, indicating a need for further research in this area.

In this study, various halide perovskite materials, including $FAPbBr_3$, $FAPbI_3$, $MAPbBr_3$, $MAPbI_3$, $CsPbBr_3$, and $CsPbI_3$, are synthesized, and their structural and chemical properties are analyzed to evaluate their suitability for use as ER fluids. To the best of our knowledge, this is the first study to compare the applicability of various halide perovskite materials in the ER. Following dispersion of the as-synthesized halide perovskite materials in silicone oil (3.0 wt % perovskite), their dispersion stabilities and dielectric properties are evaluated to confirm their potential as ER fluids. The performances of the different systems are aligned with their structures, aspect ratios, and X-site components. In addition, the synergistic effect associated with a high mechanical stability and favorable dielectric properties is examined to identify the most promising halide perovskite material for ER fluids. Additionally, $CsPbI_3$ perovskites with varying aspect ratios (L/D = 5 and 20) are prepared using the same precursor materials but different synthesis processes. The ER performances of these materials are compared, and the role of the aspect ratio is considered in terms of its ability to enhance the flow resistance and mechanical stability to support rigid fibril-like structures. This study highlights the synergistic contribution of the geometry and the dielectric properties of halide perovskite materials for enhancing the ER performance.

EXPERIMENTAL SECTION

Materials. Formamidine acetate (FAAc, 99.0%), lead(II) bromide ($PbBr_2$, 98.0%), γ-butyrolactone (GBL, 99.0%), diethyl ether (DEE, 99.0%), formamidinium iodide (FAI, 99.0%), 2-methoxy-ethanol (2-ME, 99.8%), methylammonium bromide (MABr, 99.0%), methylammonium iodide (MAI, 99.0%), and silicone oil (viscosity: 100 cSt) were purchased from Merck KGaA (Darmstadt, Germany). Hydrobromic acid (HBr, 47.0−49.0%), lead(II) iodide (PbI_2, 95.0%), cesium bromide (CsBr, 99.9%), cesium iodide (CsI, 99.9%), dimethyl sulfoxide (DMSO, 99.5%), dimethylformamide (DMF, 99.0%), toluene (99.5%), chlorobenzene (99.0%), isopropyl alcohol (IPA, 99.5%), and ethyl alcohol (EtOH, 99.5%) were acquired from Samchun Chemical Co. (Pyeongtaek, Republic of Korea). All reagents were used without additional purification process.

Synthesis of $FAPbBr_3$ and $FAPbI_3$. To synthesize $FAPbBr_3$, FAAc was dissolved in HBr to prepare a 10 M solution. Then, $PbBr_2$ powder in GBL (10 M) was added dropwise to the formamidinium acetate solution. This solution was kept in an oil bath at 90 °C for 1 h, resulting in the formation of an orange powder. The powder was collected without cooling and washed several times with DEE. Finally, the powder was baked at 150 °C.

$FAPbI_3$ was prepared by mixing FAI and PbI_2 in an equimolar ratio (1:1) in 2-ME with vigorous stirring. Subsequently, the solution was heated at 120 °C in an oil bath for 3 h, producing black $FAPbI_3$ powder. The black precipitates were filtered and washed with DEE. The filtered black $FAPbI_3$ crystals were then baked at 150 °C for 1 h and stored under N_2 conditions.

Fabrication of $MAPbBr_3$ and $MAPbI_3$. For the fabrication of $MAPbBr_3$, an equimolar ratio of MABr and $PbBr_2$ was dissolved in DMF. After stirring, the solution initially turned orange but gradually became transparent over time. The perovskite solution was then transferred to glassware containing an antisolvent (e.g., chlorobenzene), covered, and maintained at 80 °C for 3 h. As the antisolvent slowly evaporated, orange crystals began to form. The as-grown crystals were subsequently washed with DEE and dried overnight in a vacuum oven (60 °C).

To prepare $MAPbI_3$, 1 mmol of MAI was first dissolved in 1.5 mL of IPA with continuous stirring at 25 °C. Subsequently, 1 mmol of PbI_2 powder was added to the solution. Black powder was immediately formed and the mixture was stirred for an additional 30 min to stabilize the chemical reaction. After the reaction, the product was washed several times with pure IPA and dried overnight in a vacuum oven (60 °C).

Fabrication of $CsPbBr_3$ and $CsPbI_3$. For the preparation of $CsPbBr_3$, an equimolar ratio of $PbBr_2$ and CsBr was dissolved in DMSO and stirred until the solution became transparent. Then, 3.0 mL of HBr was added dropwise, which changed the color of the solution to orange. Upon completion of the addition, orange-colored powder formed. The powder

https://doi.org/10.1021/acsomega.4c11212
ACS Omega 2025, 10, 13327−13338

was collected by vacuum filtration, washed several times with EtOH, and vacuum-dried overnight (60 °C).

$CsPbI_3$ was fabricated by dissolving CsI and PbI_2 in an equimolar ratio (1:1) in DMF. Three different synthesis methods were employed for $CsPbI_3$: (i) drop-casting ($CsPbI_3$/DC), (ii) antisolvent ($CsPbI_3$/AS), and (iii) hydrothermal ($CsPbI_3$/HT), as described in the literature. (i) For drop-casting ($CsPbI_3$/DC) method, the solution was dropped onto a glass substrate and heated at 130 °C. The dried solutes were collected by scraping them off the glass surface. (ii) For antisolvent ($CsPbI_3$/AS) method, the solution was dropped into toluene, which caused the solution to become turbid. The resulting precipitates were collected, washed several times with toluene, and dried. (iii) In hydrothermal ($CsPbI_3$/HT), the solution was transferred into a Teflon-lined autoclave containing toluene and heated at 130 °C for 8 h in a muffle furnace. After cooling to room temperature, the precipitates were washed three times with toluene and dried in an oven at 130 °C. Throughout the study, $CsPbI_3$ synthesized using the drop-casting method ($CsPbI_3$/DC) was used as the standard reference.

Characterization. The crystal structures of $FAPbBr_3$, $FAPbI_3$, $MAPbBr_3$, $MAPbI_3$, $CsPbBr_3$, and $CsPbI_3$ were analyzed using X-ray diffraction (XRD, D8 Advance, Bruker Co., Billerica, MA). The phase identification of halide perovskites was performed using HighScore Plus software by searching the reference XRD database. The chemical states of the materials were examined by X-ray photoelectron spectroscopy (XPS, K-Alpha, Thermo Fisher Scientific, Waltham, MA). The sample morphologies were characterized using field-emission scanning electron microscopy (FE-SEM, S-4800, Hitachi, Tokyo, Japan). The molecular structures of samples were analyzed by a Fourier-transform infrared spectroscopy (FT-IR, Nicolet iS10, Thermo Fisher Scientific, Waltham, MA). Dielectric properties were measured with an impedance analyzer (Solartron 1260, Solartron Instruments, Hampshire, UK) equipped with a dielectric interface (Solartron 1296).

Investigation of Electrorheological (ER) Properties. To prepare ER fluids, powder $FAPbBr_3$, $FAPbI_3$, $MAPbBr_3$, $MAPbI_3$, $CsPbBr_3$, and $CsPbI_3$ samples were first ground using a mortar and pestle. The ground particles were dispersed in silicone oil by sonication for 20 min. The mixtures were then magnetically stirred for 4 h to achieve homogeneous fluid. The concentration of all ER fluids was set to 3.0 wt % without adding any additives. The ER measurement was investigated using a rheometer (MCR 102, Anton Parr, Graz, Austria) equipped with a concentric geometry (diameter: 28.0 mm, height: 30.0 mm), a cup (diameter: 30.0 mm, height: 30.0 mm), and a high-voltage generator (HCP 14-12500, FuG Elektronik GmbH, Schechen, Germany). The gap distance between the geometry and the cup was set to 1.0 mm on each side without any hindrance. A preshearing of 20.0 s^{-1} shear rate was applied for 5 min to obtain an equilibrium state of ER fluids before the measurement. After the preshearing, *E* field was applied to the system to investigate the ER properties. The ER measurement of each sample was repeated at least three times to ensure the accuracy of the data. The real-time formation of fibril-like structures of the ER fluids was observed using an optical microscope (OM, BH2-UMA, Olympus, Tokyo, Japan) equipped with a high-voltage generator (C3350, Hamamatsu, Shizuoka, Japan).

RESULTS AND DISCUSSION

Synthesis of the Halide Perovskite Materials. Figure 1 shows a schematic representation of the basic perovskite

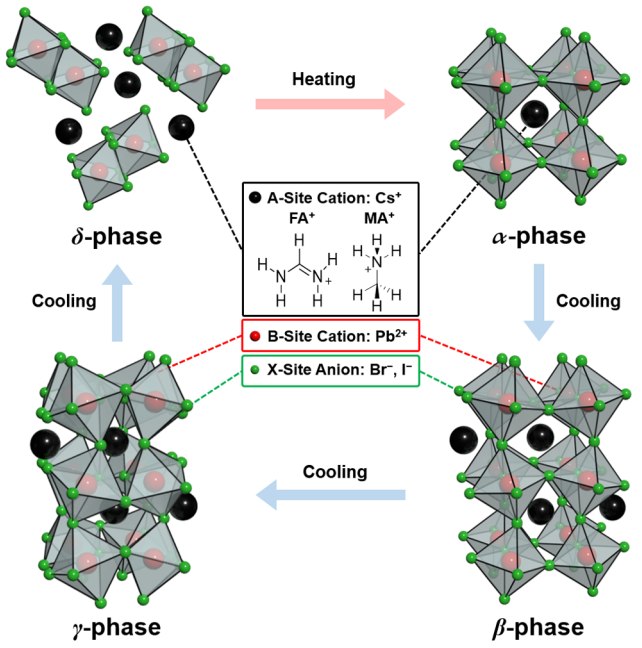

Figure 1. Schematic illustrations of various phases for halide perovskite materials with the ABX_3 formula.

structure. In the perovskite formula of ABX_3, the A-site ion is typically a larger cation, whose main role is to stabilize the structure by filling the voids created by the BX_3 network.[26] The choice of A-site ions can affect various properties of the material, such as the dielectric constant, ion conductivity, and stability, which are essential for applications in ER fluids.[27,28] In this study, formamidinium (FA^+), methylammonium (MA^+), and cesium (Cs^+) ions were selected as the A-site ions. The B-site ion, which is usually a smaller cation, coordinates with the anions at the X-sites to form an octahedral structure (BX_6). The selection of B-site cations is crucial for determining the electronic and dielectric properties of perovskites, which are important for achieving high ER performances.[29] For the purpose of this study, Pb^{2+} was chosen as the B-site cation because lead-based perovskites are known to exhibit high dielectric constants, which can enhance polarization under an *E* field.[30] The type of X-site anion also significantly affects the electronic and structural properties of perovskites. Thus, Br^- and I^- halogen ions were selected due to their tunable band gaps and high dielectric constants.[31] Additionally, halide perovskite materials can exhibit four different structures, including three perovskite structures of cubic, tetragonal, orthorhombic, and one nonperovskite structure, depending on their compositions and environmental conditions. Each of these structures demonstrates different polarizability due to their high dielectric properties, strong dipole−dipole interactions, and favorable mechanical properties, all of which contribute to the ER response.[32] As a result, six different halide perovskite materials, namely $FAPbBr_3$, $FAPbI_3$, $MAPbBr_3$, $MAPbI_3$, $CsPbBr_3$, and $CsPbI_3$ are selected as dispersing materials for the ER fluids.

The crystal structures of the prepared halide perovskite materials were examined by X-ray diffraction (XRD), and the

https://doi.org/10.1021/acsomega.4c11212
ACS Omega 2025, 10, 13327−13338

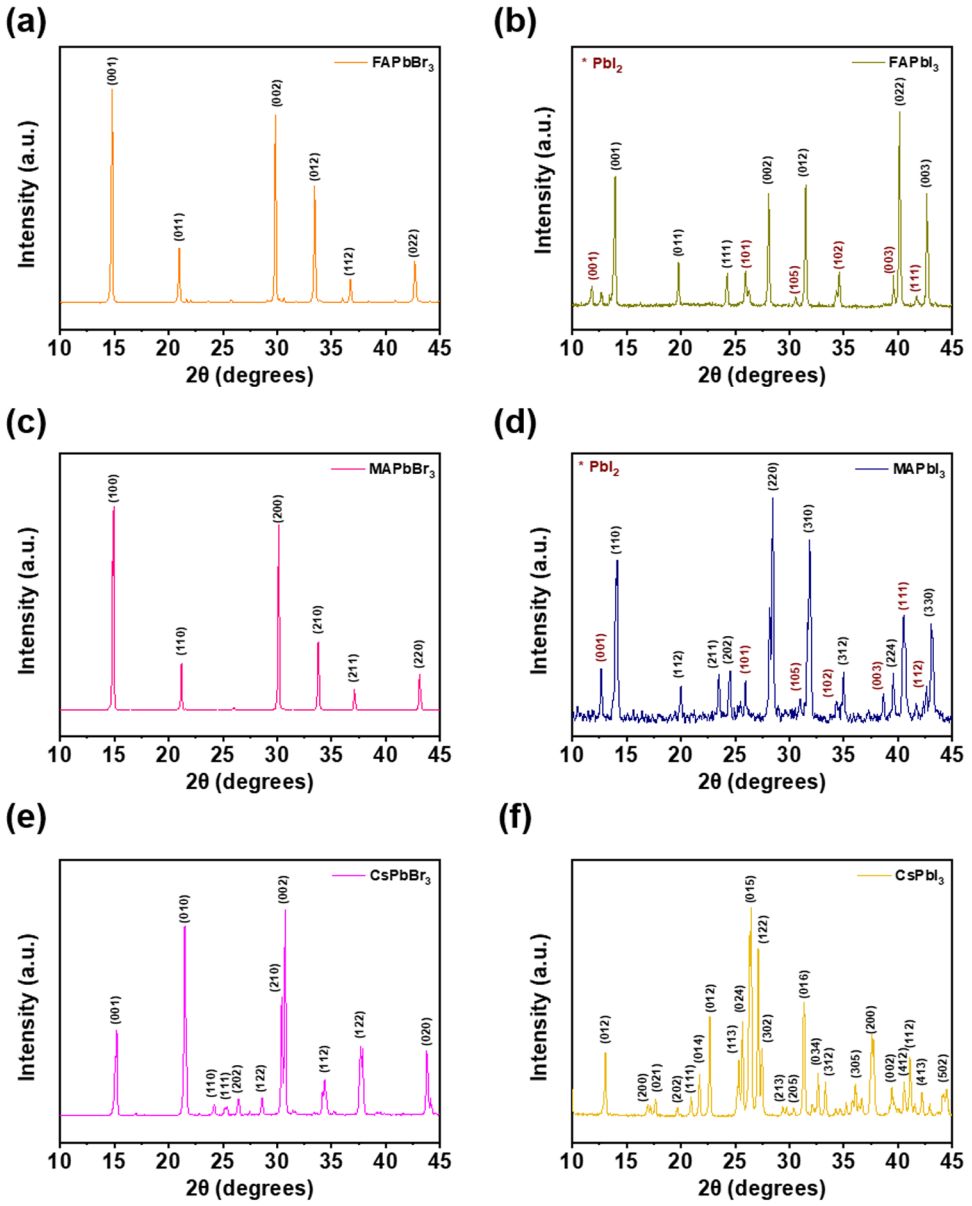

Figure 2. XRD patterns of (a) $FAPbBr_3$, (b) $FAPbI_3$, (c) $MAPbBr_3$, (d) $MAPbI_3$, (e) $CsPbBr_3$, and (f) $CsPbI_3$ materials in the 2θ range of 10−45°.

resulting spectra are shown in Figure 2. The diffraction peaks for $FAPbBr_3$ appeared at 14.8, 21.0, 29.8, 33.4, 36.8, and 42.6°, corresponding to the (001), (011), (002), (012), (112), and (022) planes of the cubic α-phase, and aligning well with reference data for cubic perovskites (Figure 2a).[33] In addition, the patterns related to the starting precursors, FAAc and HBr, matched well with the spectra, confirming the successful formation of $FAPbBr_3$. In the case of $FAPbI_3$, the diffraction peaks at 13.9, 19.8, 24.3, 28.0, 31.5, 40.2, and 42.6° corresponded to the (001), (011), (111), (002), (012), (022), and (003) planes of the α-phase (Figure 2b).[34] Additionally, peaks related to hexagonal PbI_2 (JCPDS: 873−1752) were detected due to its stronger crystallinity compared to organic components.[35,36] Notably, the sharpness of these diffraction peaks indicates the highly crystalline natures of the prepared perovskites. In the case of $MAPbBr_3$, diffraction peaks were observed at 15.0, 21.2, 30.0, 33.8, 37.1, and 43.0°, which were assigned to the (100), (110), (200), (210), (211), and (220) planes, respectively (Figure 2c).[37] Similarly, $MAPbI_3$ exhibited peaks at 14.1, 20.0, 23.4, 24.4, 28.5, 32.0, 35.0, 40.4, an 43.1°, corresponding to the (110), (112), (211), (202), (220), (310), (312), (224), and (330) crystal planes, indicating a tetragonal structure (Figure 2d).[38] As with $FAPbI_3$, PbI_2-related peaks were also detected in the patterns of $MAPbI_3$. These results confirmed the presence either α-phase cubic of FA-based halide perovskite and β-phase of tetragonal structures of MA-based halide perovskite materials. Additionally, the diffraction peaks for $CsPbBr_3$ appeared at 15.3, 21.5, 24.2, 25.4, 26.5, 28.6, 30.4, 30.8, 34.4, 37.8, and 43.8°, which align with the (001), (010), (110), (111), (202), (122), (210), (002), (112), (122), and (020) planes, respectively (Figure 2e).[39] For $CsPbI_3$, the main peaks are located at 13.1, 17.6, 22.8, 26.5, 31.4, 32.8, 37.5, 41.2, and 44.5° correlated with the (012), (021), (112), (015), (016), (034), (134), (027), and (052) planes close to the orthorhombic structure (Figure 2f).[40] Overall, the XRD patterns of each halide perovskite material matched well with

https://doi.org/10.1021/acsomega.4c11212
ACS Omega 2025, 10, 13327−13338

the reference database, confirming their distinct crystalline structures.

X-ray photoelectron spectroscopy (XPS) survey was conducted to reveal the chemical compositions of $FAPbBr_3$, $FAPbI_3$, $MAPbBr_3$, $MAPbI_3$, $CsPbBr_3$, and $CsPbI_3$, as shown in Figure 3. In the full survey spectra, each halide perovskite

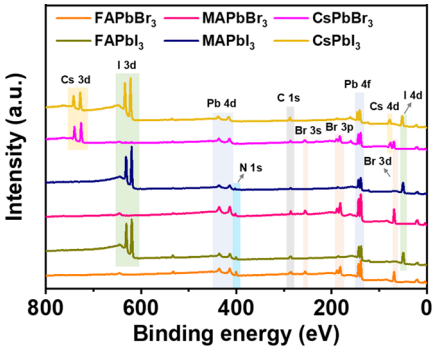

Figure 3. XPS survey spectra of $FAPbBr_3$, $FAPbI_3$, $MAPbBr_3$, $MAPbI_3$, $CsPbBr_3$, and $CsPbI_3$ materials.

material was found to contain certain elements, including N, C, Cs, Pb, Br, and I, which corresponded to their ABX_3 structures. The detailed compositions were further analyzed using high-resolution XPS. Initially, the presence of FA^+ and MA^+ was verified by observing the high-resolution N 1s and C 1s spectra, as shown in Figures S1 and S2. In the N 1s region, a single peak for $FAPbBr_3$, $FAPbI_3$, $MAPbBr_3$, and $MAPbI_3$ appeared at 400.1, 400.5, 401.7, and 401.8 eV, respectively.[41] It was clear that the binding energies of $FAPbBr_3$ and $FAPbI_3$ were lower than those of $MAPbBr_3$ and $MAPbI_3$ due to the differences in the functional groups consisting FA and MA.[42,43] Moreover, the N 1s peak for $FAPbBr_3$ and $FAPbI_3$ indicated the $C-NH_2$ group of FA, whereas that for $MAPbBr_3$ and $MAPbI_3$ corresponded to the $-NH_3^+$ group of MA.

Additionally, two distinct C 1s peaks corresponding to C−C and C−N bonds were measured.[44] Specifically, the binding energies of the C−N peaks for $FAPbBr_3$ and $FAPbI_3$ were 288.0 and 287.8 eV, respectively, which were higher than those of $MAPbBr_3$ and $MAPbI_3$ at 288.5 and 286.1 eV. These differences are attributed to variations in the binding properties between FA and MA.[45,46] Thus, N 1s and C 1s XPS results confirmed the presence of FA^+ and MA^+ in $FAPbBr_3$, $FAPbI_3$, $MAPbBr_3$, and $MAPbI_3$. Moreover, the Cs 3d XPS spectra of $CsPbBr_3$ and $CsPbI_3$ were deconvoluted into distinct Cs $3d_{3/2}$ and Cs $3d_{5/2}$ peaks at 739.0 and 725.0 eV, respectively (Figure S3).[47] These results confirmed the successful incorporation of A-site ions into the halide perovskite materials.

The B- and X-sites of the perovskite materials were further studied by analyzing their Pb 4f, Br 3d, and I 3d spectra. Figure S4 shows the high-resolution Pb 4f spectra of the halide perovskite materials. In all samples, the signals were deconvoluted into two peaks, corresponding to the Pb $4f_{5/2}$ and Pb $4f_{7/2}$ levels characteristic of perovskite materials.[48] Additionally, small peaks were observed close to the Pb^{2+} peaks, owing to the partial reduction of Pb^{2+} to Pb^0.[48] Besides the Pb 4f signals, two peaks were observed in the Pb 4d spectra, which corresponded to the Pb $4d_{3/2}$ and Pb $4d_{5/2}$ peaks.[49,50] This confirms that the B-sites of these halide perovskite materials are occupied by Pb atoms. In addition, Figure S5 shows the high-resolution Br 3d spectra of $FAPbBr_3$, $MAPbBr_3$, and $CsPbBr_3$, along with the I 3d spectra of $FAPbI_3$, $MAPbI_3$, and $CsPbI_3$. For the Br-containing materials, the spectra were deconvoluted into Br $3d_{3/2}$ and Br $3d_{5/2}$ signals, whereas for the I_3-containing materials, the spectra were deconvoluted into I $3d_{3/2}$ and I $3d_{5/2}$ peaks, thereby confirming that these materials contained either Br or I at the X-site, as appropriate.[51,52] Additionally, the detection of Br 3p, Br 3s, and I 4d peaks verified the presence of Br and I.[53,54] Accordingly, XPS analysis confirmed that the core levels of each element in the ABX_3 structure, along with their corresponding valence states, were matched with those of ideal halide perovskite structures.

The morphological structures of the prepared $FAPbBr_3$, $FAPbI_3$, $MAPbBr_3$, $MAPbI_3$, $CsPbBr_3$, and $CsPbI_3$ materials were then examined using field-emission scanning electron microscopy (FE-SEM), as shown in Figure 4. Round or

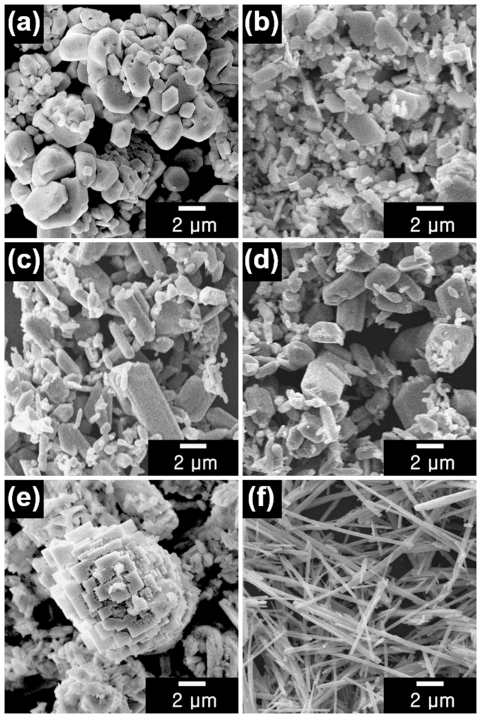

Figure 4. SEM images of the (a) $FAPbBr_3$, (b) $FAPbI_3$, (c) $MAPbBr_3$, (d) $MAPbI_3$, (e) $CsPbBr_3$, and (f) $CsPbI_3$ materials.

angular-shaped particles were uniformly observed in the Br-containing materials, including $FAPbBr_3$, $MAPbBr_3$, and $CsPbBr_3$. In addition, the particle sizes of the materials were within a few micrometers. For the I-containing materials, $FAPbI_3$ and $MAPbI_3$, hexagonal structures were observed, likely due to mixing with the hexagonal system of the precursor PbI_2 material. Particles with rod-like structures and low aspect ratios were also observed for these materials. In contrast, $CsPbI_3$ exhibited a rod-like structure with a high aspect ratio ($L/D > 10$). Accordingly, the FE-SEM results confirmed the distinctive morphologies of the as-prepared halide perovskite materials.

Furthermore, FT-IR analysis was performed to examine the molecular structures and water content of halide perovskite materials, as shown in Figure S6. In the case of $FAPbBr_3$ and $FAPbI_3$, quadruple IR bands were detected at 3394, 3331, 3256, and 3162 cm^{-1}, which corresponded to the N−H stretching vibrations of FA.[55] Also, C═N symmetric stretching

https://doi.org/10.1021/acsomega.4c11212
ACS Omega 2025, 10, 13327−13338

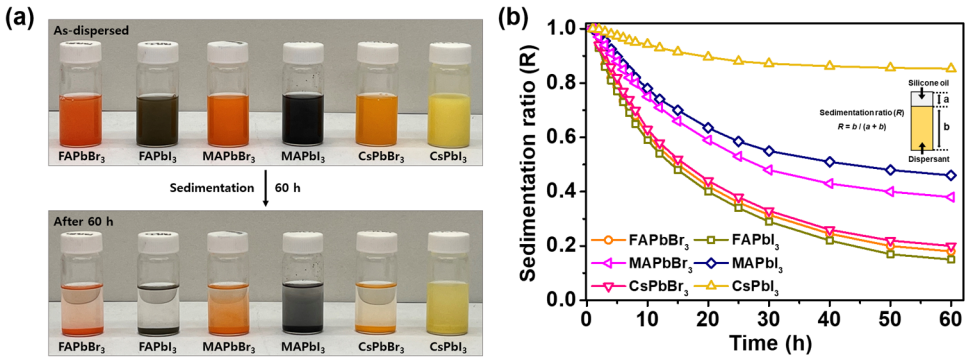

Figure 5. (a) Digital photographs of the $FAPbBr_3$-, $FAPbI_3$-, $MAPbBr_3$-, $MAPbI_3$-, $CsPbBr_3$-, and $CsPbI_3$-based ER fluids dispersed in silicone oil (3.0 wt %). The top image shows the initial state, while the bottom image shows the samples after sedimentation for 60 h. (b) Dispersion stabilities of the halide perovskite-based ER fluids as a function of the sedimentation time.

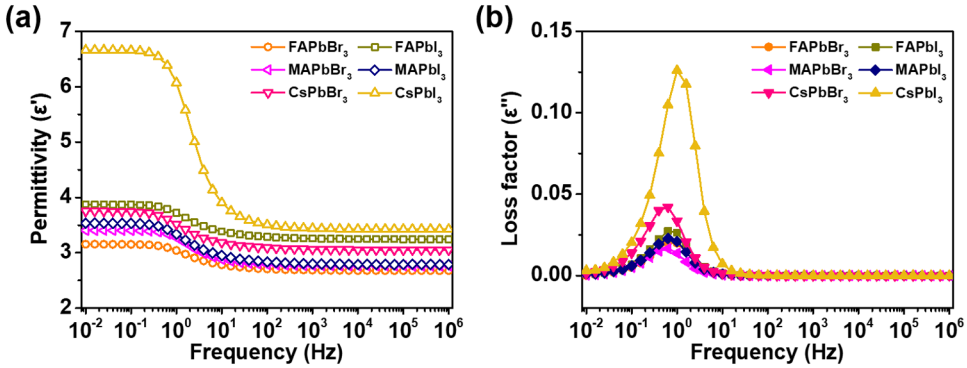

Figure 6. (a) Permittivity values and (b) loss factors as a function of the E field frequency for the $FAPbBr_3$-, $FAPbI_3$-, $MAPbBr_3$-, $MAPbI_3$-, $CsPbBr_3$-, and $CsPbI_3$-based ER fluids.

vibrations was detected at 1706 cm^{-1}, confirming the presence of FA cation.[55] For $MAPbBr_3$ and $MAPbI_3$, MA-related peaks were observed. In detail, peaks located at 2913, 2822, 1570, 959, and 903 cm^{-1} corresponded to the $-NH_3$ stretching, $-CH_3$ stretching, $-$ NH_3 bending, C−N stretching, and C−H bending vibrations, respectively.[56−58] In the case of $CsPbBr_3$ and $CsPbI_3$, no specific peaks were revealed due to the dominance of ionic bonds over covalent bonds. The water content of sample was evaluated by observing the −OH peak in the range between 3200 and 3600 cm^{-1}. For all halide perovskite materials, there was no broad peak detected in the range of −OH, verifying the minimal water content under our experimental conditions including synthesis conditions and storing conditions in a desiccator.

Suitability of the Various Halide Perovskite Materials for ER Applications. To prepare the ER fluids, various halide perovskite materials, including $FAPbBr_3$, $FAPbI_3$, $MAPbBr_3$, $MAPbI_3$, $CsPbBr_3$, and $CsPbI_3$, were initially dispersed in silicone oil at a concentration of 3.0 wt % and mixed thoroughly. The suitability of each ER fluid was evaluated by analyzing the dispersion stability and dielectric properties, both of which are crucial in the context of ER applications. Initially, the dispersion stability was examined (Figure 5). In ER applications, maintaining a high dispersion stability without sedimentation is essential, as it helps preserve the fibril-like structures formed under an applied E field.[59] In the initial state, all particles were found to be uniformly dispersed in the medium; however, they gradually sedimented over time until reaching an equilibrium state. The sedimentation ratio (R) is defined as the height of the dispersed materials (b) divided by the total height of the fluid ($a + b$), as expressed by the following formula.

$$\text{sedimentation ratio}(R) = b/(a + b) \quad (1)$$

Among the prepared ER fluids, the $CsPbI_3$-based ER fluid exhibited an exceptional sedimentation ratio of 0.85 even after 60 h. This can be attributed to the geometrical effect of its rod-like structure with a high aspect ratio ($L/D > 10$), which led to an increased flow resistance in the orthorhombic or non-perovskite phases.[24,60] Consequently, a greater degree of friction is created in the medium, thereby reducing sedimentation. For the various ER fluids, the dispersion stability followed the order: $CsPbI_3$ > $MAPbI_3$ > $MAPbBr_3$ > $CsPbBr_3$ > $FAPbBr_3$ > $FAPbI_3$. Consequently, $CsPbI_3$ was considered optimal for use as a dispersing material for ER fluids owing to its enhanced dispersion stability.

The dielectric properties of the halide perovskite materials were evaluated to confirm their suitability for use in ER applications. Specifically, materials with high dielectric properties can provide interfacial polarization, known as Maxwell−Wagner−Sillars polarization, at the interface between the dispersed particles and the medium when an E field is applied.[61,62] This polarization allows materials to readily form fibril-like structures through electrostatic interactions, thereby exhibiting higher ER activities than materials with lower dielectric properties.[63] To investigate the polarizability characteristics of the halide perovskite materials, their dielectric properties were analyzed by measuring the dielectric constant (or permittivity, ε') and loss factor (ε'') at an applied E field strength of 3.0 kV mm^{-1}, as shown in Figure 6. Two dominant

https://doi.org/10.1021/acsomega.4c11212
ACS Omega 2025, 10, 13327−13338

factors for ER performance, namely the achievable polarizability ($\Delta\varepsilon$) and the relaxation time (λ), were obtained from the permittivity and loss factor curves. The former was determined by subtracting the permittivity at a high frequency from that at a low frequency, thereby indicating the degree of material polarization.[64] The relaxation time was calculated by first identifying the frequency at which the loss factor reached its maximum, and then applying the following equation.[65]

$$\lambda = \frac{1}{2\pi f_{max}} \quad (2)$$

Previous studies have reported that a high ER performance is associated with materials that possess larger $\Delta\varepsilon$ and shorter λ, as these properties increase the degree of polarizability and allow for a faster polarization response when an external E field is applied to the ER fluid.[24,65] Thus, the dielectric parameters for the $FAPbBr_3$-, $FAPbI_3$-, $MAPbBr_3$-, $MAPbI_3$-, $CsPbBr_3$-, and $CsPbI_3$-based ER fluids were determined and are summarized in Table 1. Among them, the $CsPbI_3$-based ER fluid showed the highest $\Delta\varepsilon$ (3.24) and shorter λ (0.14 s) values compared to the other perovskite materials. Specifically, $CsPbI_3$ exhibited high polarization at low frequencies due to the formation of large polarons arising from the larger size of I^- ions, which induce distortion in the PbX_6 octahedral framework and change the electronic charge distribution.[66] At high frequencies, the charge carriers not respond quickly to the rapidly changing field, resulting in a decrease of polarization. Also, the high polarization can be attributed to the advantages of using an inorganic atom as the A-site, the distorted and asymmetric structure that enhances polarization, and the geometric benefit of a rod-like morphology with a high aspect ratio.[25,67] These results indicate that $CsPbI_3$ has several advantages over other perovskite materials, rendering it a suitable dispersion material for ER applications.

Table 1. Dielectric Parameters of Various Perovskite-Based ER Fluids[a]

sample	ε_o	ε_∞	$\Delta\varepsilon$[b]	f_{max}[c] (Hz)	λ[d] (s)
$FAPbBr_3$	3.15	2.68	0.47	0.76	0.21
$FAPbI_3$	3.87	3.24	0.63	0.78	0.20
$MAPbBr_3$	3.40	2.76	0.64	0.65	0.24
$MAPbI_3$	3.53	2.79	0.74	0.68	0.23
$CsPbBr_3$	3.74	3.05	0.69	0.55	0.29
$CsPbI_3$	6.66	3.42	3.24	1.13	0.14

[a]The dielectric properties were obtained using a Solartron SI 1260 impedance analyzer with a Solartron 1296 dielectric interface. [b]The difference between ε_o and ε_∞ ($\Delta\varepsilon = \varepsilon_o - \varepsilon_\infty$) is associated with the achievable polarizability. [c]The local frequency at which the dielectric loss factor (ε'') is maximized was evaluated by nonlinear regression analysis using OriginPro. [d]The relaxation time was determined by $\lambda = 1/(2\pi f_{max})$, where f_{max} is the frequency of the dielectric loss factor peak.

Electrorheological Properties of the Halide Perovskite-Based ER Fluids. The ER performances of the $FAPbBr_3$-, $FAPbI_3$-, $MAPbBr_3$-, $MAPbI_3$-, $CsPbBr_3$-, and $CsPbI_3$-based ER fluids were investigated by measuring the shear stress as a function of the shear rate under E field on/off conditions and as a function of the E field strength. The ER fluids were prepared by dispersing the various perovskite materials in silicone oil at a 3.0 wt % concentration. Prior to applying an external E field, the shear stress and viscosity curves of the ER fluids in the zero-field state were evaluated (Figure 7a). In the absence of an E field, all ER fluids displayed typical Newtonian behavior, producing shear stress curves proportional to the shear rate.[68] However, the viscosities decreased with an increasing shear rate, indicating the presence of shear-thinning behavior.[69] Among them, the $CsPbI_3$-based ER fluid exhibited a slightly higher shear stress and viscosity owing to the increased flow resistance of the rod-like structure.[70] Under a constant E field strength of 3.0 kV mm^{-1}, the ER activities were analyzed by measuring the shear stress and viscosity as a function of the shear rate, as shown in Figure 7b. When the E field was applied, all ER fluids instantly exhibited stress, indicating the formation of fibril-like structures caused by electrostatic forces between the dispersed particles in the medium.[71] In the low-shear-rate region, Bingham plastic behavior was observed, which was dominated by the electrostatic forces between the particles under the E field, surpassing the hydrodynamic forces generated by rotational shearing.[4,72] Beyond a certain critical shear rate (γ_c), the hydrodynamic forces overwhelmed the electrostatic forces, resulting in Newtonian behavior and breaking down the chain-like structures.[3] Among the fluids, only $CsPbI_3$-based ER fluid demonstrated an acceptable ER performance. More specifically, the measured shear stresses for the $FAPbBr_3$-, $FAPbI_3$-, $MAPbBr_3$-, $MAPbI_3$, $CsPbBr_3$-, and $CsPbI_3$-based ER fluids under an E field strength of 3.0 kV mm^{-1} were ca. 3.6, 5.8, 4.0, 4.4, 5.0, and 99.4 Pa, respectively. This exceptional high performance for the $CsPbI_3$-based ER fluid was attributed to the synergistic effects of the high dielectric properties for polarization and the enhanced dispersion stability owing to the geometrical advantage of the rod-like structures.[9,24]

A real-time E field on/off test was conducted to verify the reversibility characteristics of the ER fluids based on the different halide perovskite materials, as shown in Figure 7c. In the absence of an E field, low yield stress values of <1.0 Pa were observed for all ER fluids, indicating their resting state. Upon applying an E field strength of 3.0 kV mm^{-1}, immediate yield stresses were detected for all ER fluids, which increased in the order $FAPbBr_3$ < $MAPbBr_3$ < $MAPbI_3$ < $CsPbBr_3$ < $FAPbI_3$ < $CsPbI_3$, thereby indicating that the dispersion stability and dielectric properties influenced the ER performance. When the applied E field was removed, the yield stresses instantly returned to their initial states, confirming the reversible and fast response characteristics of the ER fluids. Furthermore, the dynamic yield stresses of the ER fluids based on the halide perovskite materials were evaluated as a function of the E field strength, ranging from 0.5 to 3.0 kV mm^{-1} at a fixed shear rate of 0.1 s^{-1} (Figure 7d). For the $CsPbI_3$-based ER fluid, the dynamic yield stress was proportional to the square of the E field, whereas proportional but less steep relationships were observed for the other ER fluids. These results verify that the yield stress of the $CsPbI_3$-based ER fluid increased more rapidly with an increasing E field strength owing to its high dielectric properties and dispersion stability.[73,74] Overall, the experimental results highlighted the advantages of using $CsPbI_3$ as a dispersing material in ER fluids.

Optical microscopy (OM) analysis was performed to visually reveal the real-time responses of the $FAPbBr_3$-, $FAPbI_3$-, $MAPbBr_3$-, $MAPbI_3$-, $CsPbBr_3$-, and $CsPbI_3$-based ER fluids under an E field strength of 3.0 kV mm^{-1} (Figure 8). With the absence of an E field, the particles were randomly distributed in the silicone oil without aggregation, while upon application

https://doi.org/10.1021/acsomega.4c11212
ACS Omega 2025, 10, 13327−13338

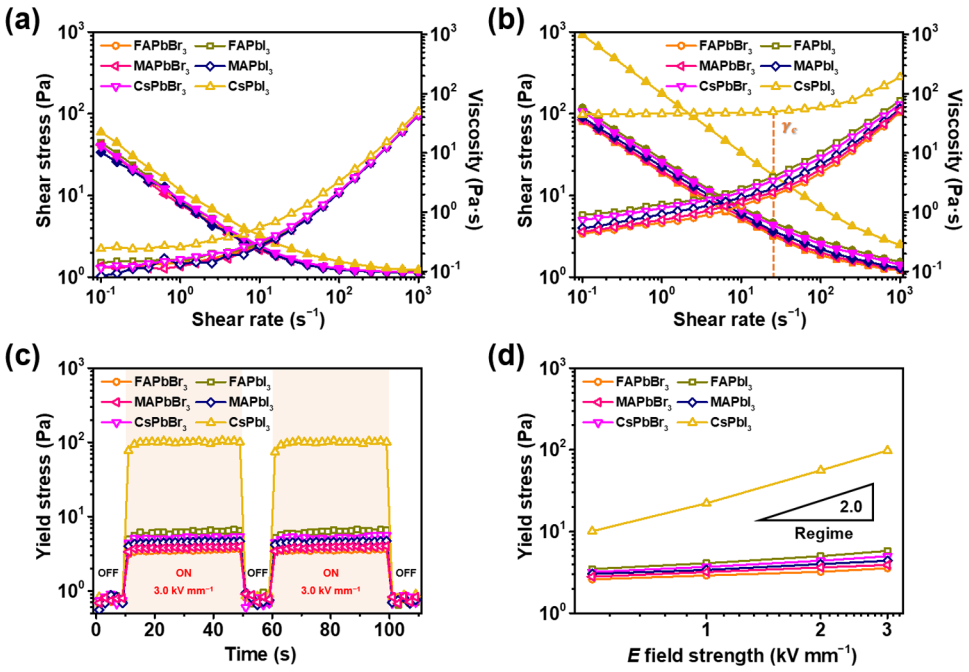

Figure 7. (a) Zero-field shear stress (open) and viscosity (solid) curves recorded for the $FAPbBr_3$-, $FAPbI_3$-, $MAPbBr_3$-, $MAPbI_3$-, $CsPbBr_3$-, and $CsPbI_3$-based ER fluids (3.0 wt %) as a function of the shear rate and in the absence of an applied E field. (b) Flow curves and viscosities of the various halide perovskite-based ER fluids under an E field strength of 3.0 kV mm^{-1}. (c) E field on/off tests performed for the ER fluids at a fixed shear rate of 0.1 s^{-1}. (d) Dynamic yield stress results for the ER fluids as a function of the E field strength from 0.5 to 3.0 kV mm^{-1}.

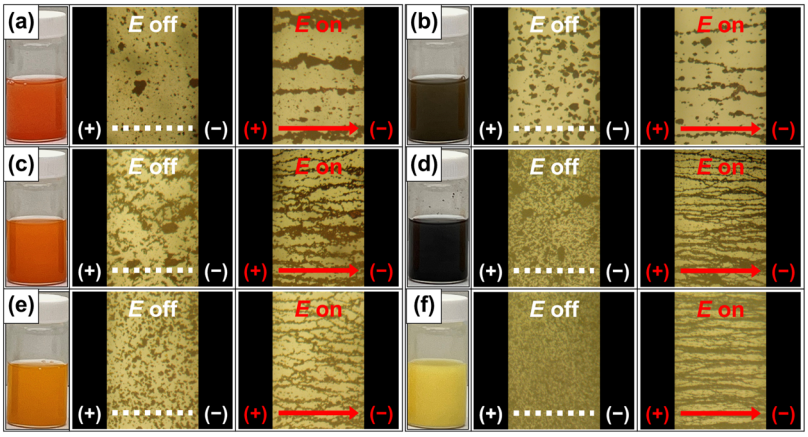

Figure 8. Optical microscopy (OM) images for the formation of fibril-like structures in the (a) $FAPbBr_3$-, (b) $FAPbI_3$-, (c) $MAPbBr_3$-, (d) $MAPbI_3$-, (e) $CsPbBr_3$-, and (f) $CsPbI_3$-based ER fluids (3.0 wt %) under an E field strength of 3.0 kV mm^{-1}. The gap distance between two electrodes was set to 1.0 mm.

of the E field, the dispersed particles rapidly formed fibril-like structures aligned in the E field direction. The densest formation of fibril-like structures was observed for the $CsPbI_3$-based ER fluid, as indicated by the darkened areas. These observations clearly confirm the rigidity of its solid-like structure. In contrast, the other ER fluids exhibited less-rigid structures owing to their lower degrees of polarization. Overall, the OM observations confirmed the rapid responsiveness and reversible properties of the ER fluids.

Finally, rod-like $CsPbI_3$ materials with different aspect ratios (L/D) were prepared by altering the synthesis method, and their ER activities were compared to further confirm the effect of the sample geometry on the ER performance. Thus, in addition to the drop-casting method ($CsPbI_3$/DC), the antisolvent ($CsPbI_3$/AS) and hydrothermal ($CsPbI_3$/HT) methods were applied using the same precursor material.[75] Based on SEM observations, the aspect ratio of $CsPbI_3$/AS was measured to be 5, which is lower than that of the $CsPbI_3$/DC specimen (L/D = 10). In addition, the aspect ratio of the $CsPbI_3$/HT sample was 20, which is higher than that of $CsPbI_3$/DC (Figure S7). To evaluate the effect of the aspect ratio on the ER performance, both $CsPbI_3$/AS and $CsPbI_3$/HT were dispersed in silicone oil (3.0 wt %) to prepare their corresponding ER fluids. Initially, the rheological properties were observed in the absence of an applied field. As shown in Figure 9a, the shear stress and viscosity were proportional to the shear rate under these conditions. Notably, the $CsPbI_3$/HT-based ER fluid exhibited a higher stress and viscosity, suggesting that rod-like materials with higher aspect ratios exhibit enhanced shear stresses owing to their increased mechanical stabilities and flow resistances.[76] Upon the application of an E field (3.0 kV mm^{-1}), all $CsPbI_3$-based

https://doi.org/10.1021/acsomega.4c11212
ACS Omega 2025, 10, 13327−13338

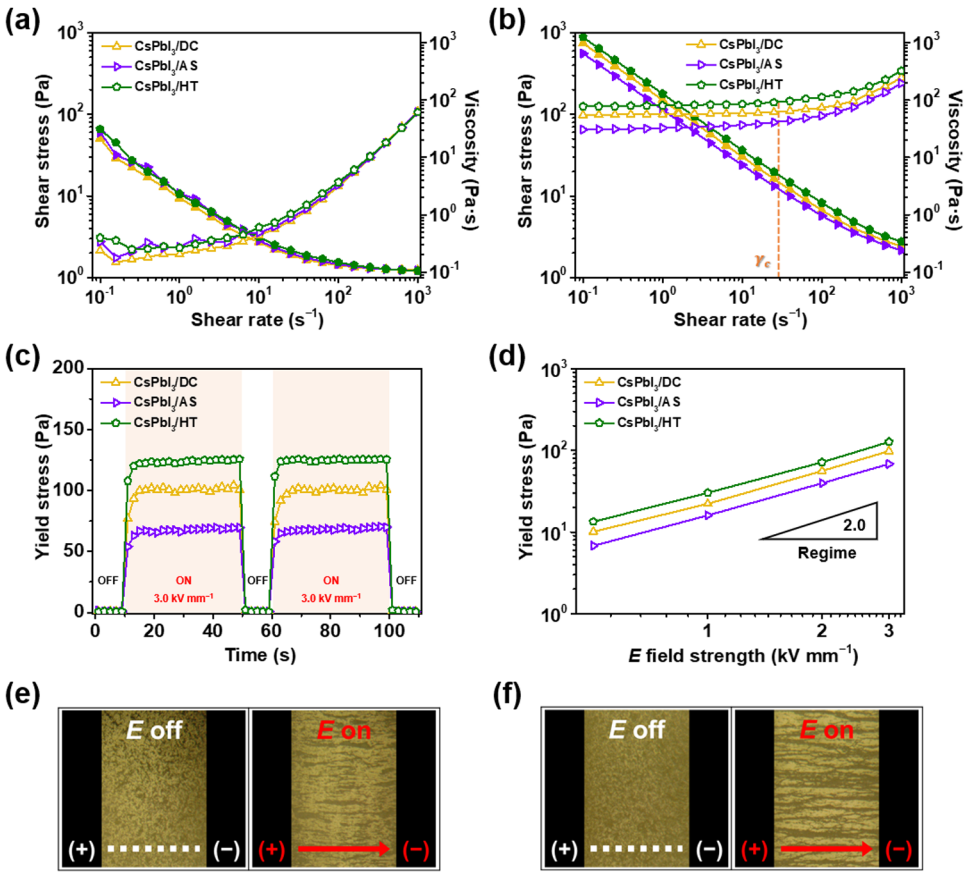

Figure 9. (a) Zero-field shear stress (open) and viscosity (solid) curves recorded for the $CsPbI_3$/DC-, $CsPbI_3$/AS-, and $CsPbI_3$/HT-based ER fluids (3.0 wt %) as a function of the shear rate in the absence of an applied *E* field. (b) Shear stress and viscosity curves recorded for the various $CsPbI_3$-based ER fluids as a function of the shear rate under an *E* field strength of 3.0 kV mm^{-1}. (c) Reversibility tests performed for the different $CsPbI_3$-based ER fluids by switching the *E* field (3.0 kV mm^{-1}) on and off at a constant shear rate (0.1 s^{-1}). (d) Yield stress as a function of the applied *E* field strength at a 0.1 s^{-1} shear rate. OM images showing the formation of fibril-like structures for the (e) $CsPbI_3$/AS- and (f) $CsPbI_3$/HT-based ER fluids under an *E* field strength of 3.0 kV mm^{-1}.

ER fluids displayed constant shear stresses, with Bingham plastic behavior being observed (Figure 9b). The ER performance was ranked in the order $CsPbI_3$/AS < $CsPbI_3$/DC < $CsPbI_3$/HT, with corresponding shear stress values of ca. 71.0, 99.4, and 128.0 Pa, respectively. Notably, these values increased in the same order as the sample aspect ratios. Additionally, as presented in Figure 9c,d, the ER on/off and *E* field strength tests confirmed the reversibility, fast response, and *E* field-dependent behaviors of the prepared fluids. OM analysis further verified the formation of strong chain-like structures upon the application of a specific *E* field strength (i.e., 3.0 kV mm^{-1}, Figure 9e,f). Accordingly, it was confirmed that the geometrical effect of the aspect ratio further contributed to the enhanced ER performances of $CsPbI_3$-based ER fluids.

CONCLUSIONS

In conclusion, six halide perovskite materials, namely $FAPbBr_3$, $FAPbI_3$, $MAPbBr_3$, $MAPbI_3$, $CsPbBr_3$, and $CsPbI_3$, which are commonly used in solar cells, were synthesized for use as dispersing materials in electrorheological (ER) fluids. To the best of our knowledge, this is the first study comparing the applicability of halide perovskite materials in ER. Various morphological and chemical analyses confirmed the successful formation of halide perovskite structures, with $CsPbI_3$ exhibiting a rod-like structure with a high aspect ratio (*L*/*D* = 10). After dispersing the halide perovskite materials in silicone oil (3.0 wt %), their dispersion stabilities and dielectric properties were evaluated. Among them, the $CsPbI_3$-based ER fluid exhibited the highest sedimentation ratio (0.85), highest achievable polarizability ($\Delta\varepsilon$ = 3.24), and shortest relaxation time (0.14 s), demonstrating its strong potential for use in ER applications. In addition, the $CsPbI_3$-based ER fluid exhibited the highest ER performance (99.4 Pa), which was attributed to the synergistic effect of the mechanical stability originating from the rod-like structures and the high dielectric properties for polarization. To investigate the effect of the particle size on the ER activity, the aspect ratio of $CsPbI_3$ was modified by altering the synthesis method. Consequently, the $CsPbI_3$-based ER fluid synthesized via the hydrothermal method with an aspect ratio of 20 demonstrated an exceptionally high ER performance of 128.0 Pa. The results of this study highlights the potential of employing halide perovskite materials in ER applications, suggesting future pathways for their use in various fields.

ASSOCIATED CONTENT

Supporting Information

The Supporting Information is available free of charge at https://pubs.acs.org/doi/10.1021/acsomega.4c11212.

High-resolution N 1s XPS spectra; High-resolution C 1s XPS spectra; High-resolution Cs 3d XPS spectra; High-

https://doi.org/10.1021/acsomega.4c11212
ACS Omega 2025, 10, 13327−13338

resolution Pb 4f XPS spectra; High-resolution Br 3d and I 3d XPS spectra; FT-IR spectra; and SEM images of various $CsPbI_3$ materials (PDF)

AUTHOR INFORMATION

Corresponding Authors

Seulki Song − *Department of Chemical Engineering and Applied Chemistry, Chungnam National University, Daejeon 34134, Korea*; Email: sksong@cnu.ac.kr

Chang-Min Yoon − *Department of Chemical and Biological Engineering, Hanbat National University, Daejeon 34158, Korea; Department of Polymer Science and Engineering, Inha University, Incheon 22212, Korea*; orcid.org/0000-0002-6530-3833; Phone: +82-42-821-1528; Email: cmyoon4321@hanbat.ac.kr, cmyoon4321@inha.ac.kr; Fax: +82-42-821-1593

Authors

Suk Jekal − *Department of Chemical and Biological Engineering, Hanbat National University, Daejeon 34158, Korea; Department of Polymer Science and Engineering, Inha University, Incheon 22212, Korea*

Hyuntae Choi − *Department of Chemical Engineering and Applied Chemistry, Chungnam National University, Daejeon 34134, Korea*

Zambaga Otgonbayar − *Department of Chemical and Biological Engineering, Hanbat National University, Daejeon 34158, Korea; Department of Polymer Science and Engineering, Inha University, Incheon 22212, Korea*

Jiwon Kim − *Department of Chemical and Biological Engineering, Hanbat National University, Daejeon 34158, Korea; Department of Polymer Science and Engineering, Inha University, Incheon 22212, Korea*

Yoon-Ho Ra − *Department of Chemical and Biological Engineering, Hanbat National University, Daejeon 34158, Korea; Department of Polymer Science and Engineering, Inha University, Incheon 22212, Korea*

Jeongin Lim − *Department of Chemical Engineering and Applied Chemistry, Chungnam National University, Daejeon 34134, Korea*

Young Un Jeon − *Department of Chemical Engineering and Applied Chemistry, Chungnam National University, Daejeon 34134, Korea*

Jeoung Han Kim − *Department of Materials Science and Engineering, Hanbat National University, Daejeon 34158, Korea*

Jinsung Rho − *Department of Mechanical Engineering, Hanbat National University, Daejeon 34158, Korea*; orcid.org/0000-0002-4525-8860

Complete contact information is available at: https://pubs.acs.org/10.1021/acsomega.4c11212

Author Contributions

[⊥]S.J. and H.C. contributed equally to this work.

Notes

The authors declare no competing financial interest.

ACKNOWLEDGMENTS

This research was supported by the HBNU 2024 KNUDP (Korea National University Development Project) funded by the Ministry of Education (MOE, Korea) and National Research Foundation of Korea (NRF).

REFERENCES

(1) Halsey, T. C. Electorheological Fluids. *Science* **1992**, *258*, 761−766.

(2) Agresti, F.; Isopi, J.; Marchese, S. S.; Giorgianni, P.; Contino, A.; Marchese, S. S.; Titov, I.; Rancan, M.; Armelao, L.; Barison, S. Electrorheology of urea-functionalized lathlike goethite particles in silicone oil. *Colloids Surf., A* **2025**, *704*, No. 135509.

(3) Jekal, S.; Sa, M.; Chu, Y.-R.; Kim, C.-G.; Noh, J.; Kim, J.; Kim, H.-Y.; Oh, W.-C.; Otgonbayar, Z.; Yoon, C.-M. A Study on Enhanced Electrorheological Performance of Plate-like Materials via Percolation Gel-like Effect. *Gels* **2023**, *9*, 891.

(4) Jekal, S.; Kim, J.; Lu, Q.; Kim, D.-H.; Noh, J.; Kim, H.-Y.; Kim, M.-J.; Kim, M.-S.; Oh, W.-C.; Choi, H.-J.; Yoon, C.-M. Development of Novel Colorful Electrorheological Fluids. *Nanomaterials* **2022**, *12*, No. 3113.

(5) Noh, J.; Jekal, S.; Kim, J.; Kim, H.-Y.; Chu, Y.-R.; Kim, C.-G.; Oh, W.-C.; Song, S.; Sim, H. S.; Yoon, C.-M. Vivid-Colored Electrorheological fluids with simultaneous enhancements in color clarity and Electro-Responsivity. *J. Colloid Interface Sci.* **2024**, *657*, 373−383.

(6) Kang, P.; Liu, S.; Zeng, T. Magnetorheological Fluid-Based Haptic Feedback Damper. *Appl. Sci.* **2024**, *14*, No. 3697.

(7) Yao, Y.; Wang, X.; Liu, Z. Investigation on influence factors of optically controlled electrorheological fluid damping system. *Smart Mater. Struct.* **2024**, *33*, No. 125018.

(8) Soares, J. P.; Gomes, K. P. D.; Soares, B. G. Acidic phosphonium-based ionic liquid encapsulated on titania particles with enhanced electrorheological response. *Colloids Surf., A* **2025**, *705*, No. 135651.

(9) Dong, Y.; Wang, Y.; Liu, Y.; Ding, B.; Li, Y.; Li, Z.; Sun, L.; Yin, J. Interfacial polarization and electrorheological effect of homo-poly(ionic liquid) and poly(ionic liquid)-hexyl methacrylate copolymer microsphere particles. *Polymer* **2024**, *299*, No. 126970.

(10) Calis-Ismetoglu, G.; Cevher, S. C.; Unal, H. I. Probing effect of counterions on electric field stimuli responsive behaviours of smart organoboron-based polyelectrolytes. *React. Funct. Polym.* **2024**, *201*, No. 105947.

(11) Wang, L.; Chen, L.; Yan, H.; Wang, C.; Lin, Y.; Wang, B.; Hao, C. Synthesis and electrorheological behaviour of silica-coated porous metal-organic frameworks. *Ceram. Int.* **2024**, *50*, 11329−11340.

(12) Zhang, W. L.; Liu, Y. D.; Choi, H. J. Graphene oxide nanocomposites and their electrorheology. *Mater. Res. Bull.* **2013**, *48*, 4997−5002.

(13) Chen, T.; Wang, J.; Li, X.; Chen, Y.; Liu, S.; Liu, Z.; You, Q.; Liu, X.; Chen, F.; Liu, J. High dielectric transparent polymer composite with well-organized carboxymethyl cellulose microfibers in silicon elastomer fabricated under direct current electric field. *Carbohydr. Polym.* **2024**, *329*, No. 121803.

(14) Yin, J.-B.; Zhao, X.-P. Preparation and electrorheological characteristics of Y-doped $BaTiO_3$ suspension under dc electric field. *J. Solid State Chem.* **2024**, *177*, 3650−3659.

(15) Gollino, L.; Leblanc, A.; Dittmer, J.; Mercier, N.; Pauporté, T. New Dication-Based Lead-Deficient 3D $MAPBI_3$ and $FAPBI_3$ "d-HPs" Perovskites with Enhanced Stability. *ACS Omega* **2023**, *8*, 23870−23879.

(16) Ria, M. S. I.; Ghosh, A.; Rahman, M. A.; Al-Humal, J. Y.; Awwad, N. S.; Ibrahium, H. A.; Rahman, M. M. Examining anion influence on the physical properties and performance analysis of lead-free calcium-based Ca_3NX_3 (X = F, Cl, Br and I) perovskite. *Mater. Sci. Eng.* **2024**, *310*, No. 117674.

(17) Raman, T. S. A.; Arun, B.; Chivakumar, C.; Joseph, A.; Raju, K. C. J. Influence of oxygen pressure during deposition on the microwave dielectric tunability of $Ba_{0.5}Sr_{0.5}TiO_3$ thin films in PLD process. *Appl. Surf. Sci.* **2024**, *669*, No. 160477.

(18) Gamal, K.; Gamal, M.; Okaz, A.; Shehata, N.; Kandas, I. Comprehensive performance analysis of perovskite solar cells based on different crystalline structures of $MAPbI_3$. *Opt. Quantum Electron.* **2024**, *56*, 827.

(19) Rahmany, S.; Dayan, A. S.; Wierzbowska, M.; Ong, A. J.; Li, Y.; Magdassi, S.; Tok, A. L. Y.; Etgar, L. The Impact of Piezoelectricity in Low Dimensional Metal Halide Perovskite. *ACS Energy Lett.* **2024**, *9*, 1527−1536.
(20) Butler, K. T. The chemical forces underlying octahedral tilting in halide perovskites. *J. Mater. Chem. C* **2018**, *6*, 12045−12051.
(21) Gong, Y.-J.; Li, Z.-G.; Guo, T.-M.; Zhao, C.; Zhang, Y.; He, M.; Yu, J.; Li, W.; Bu, X.-H. Programming Piezoelectric Phase of Poly(Vinylidene Fluoride) via Hybrid Metal Halide Perovskite for Enhanced Electromechanical Performance. *Adv. Energy Mater.* **2024**, *14*, No. 2400241.
(22) Kovaleva, V. V.; Kuznetsov, N. M.; Istomina, A. P.; Bogdanova, O. I.; Vdovichenko, A. Y.; Streltsov, D. R.; Malakhov, S. N.; Kamyshinsky, R. A.; Chvalun, S. N. Low-filled suspensions of α-chitin nanorods for electrorheological applications. *Carbohydr. Polym.* **2022**, *277*, No. 118792.
(23) Yin, J.; Zhao, X. Electrorheology of nanofiber suspensions. *Nanoscale Res. Lett.* **2011**, *6*, No. 256.
(24) Yoon, C.-M.; Lee, K.; Noh, J.; Lee, S.; Jang, J. Electrorheological performance of multigram-scale mesoporous silica particles with different aspect ratios. *J. Mater. Chem. C* **2016**, *4*, 1713−1719.
(25) Noh, J.; Yoon, C.-M.; Jang, J. Enhanced electrorheological activity of polyaniline coated mesoporous silica with high aspect ratio. *J. Colloid Interface Sci.* **2016**, *470*, 237−244.
(26) Wang, Q.; Zheng, X.; Deng, Y.; Zhao, J.; Chen, Z.; Huang, J. Stabilizing the α-Phase of $CsPbI_3$ Perovskite by Sulfobetaine Zwitterions in One-Step Spin-Coating Films. *Joule* **2017**, *1*, 371−382.
(27) Ullah, M.; Ullah, N.; Tighezza, A. M.; Bashir, B.; Batool, K.; Murtaza, G. Bandgap Nature Transition and the Optical Properties of ABX_3 (A = K, Rb; B = Sr, Ba, Ca; X = Cl, Br, I) Perovskites under Pressure. *J. Inorg. Organomet. Polym. Mater.* **2025**, *35*, 552−569.
(28) Okumura, R.; Oku, T.; Suzuki, A. Electronic structures of ABX_3 perovskite crystals with a monovalent copper ion as the A-site cation. *Chem. Phys. Impact* **2024**, *8*, No. 100534.
(29) Yang, X.; Fernández−Carrión, A. J.; Geng, X.; Kuang, X. *B*-site deficient hexagonal perovskites: Structural stability, ionic order-disorder and electrical properties. *Prog. Solid State Chem.* **2024**, *74*, No. 100459.
(30) Li, J.; Hu, D.; Chen, Q. Pb^{2+}/Co^{2+} modified growth and phase transitions of $CsPbBr_3$ in heavy metal oxide glass with enhanced magnetic and magneto-optical properties. *J. Eur. Ceram. Soc.* **2024**, *44*, 2206−2222.
(31) Shi, J.; Deng, H.; Liu, F.; Li, R.; Qiu, X.; Tu, Y.; Wu, L.; Xu, Y.; Tian, J.; Zhu, C.; Wu, J.; Lan, Z. Polar Species Modified Dielectric Constant of $CsPbI_2Br$ Perovskite Nanocrystals: Implications for Carbon-Based Perovskite Solar Cells. *ACS Appl. Nano Mater.* **2024**, *7*, 14363−14371.
(32) Minussi, F. B.; Silva, R. M.; Araújo, E. B. Composition-Property Relations for $GA_xFA_yMA_{1-x-y}PbI_3$ Perovskites. *Small* **2024**, *20*, No. 2305054.
(33) Zhang, F.; Yang, B.; Zheng, K.; Yang, S.; Li, Y.; Deng, W.; He, R. Formamidinium Lead Bromide ($FAPbBr_3$) Perovskite Microcrystals for Sensitive and Fast Photodetectors. *Nano-Micro Lett.* **2018**, *10*, No. 43.
(34) Murugadoss, G.; Arunachalam, P.; Panda, S. K.; Kumar, M. R.; Rajabathar, J. R.; Al-Lohedan, H.; Wasmiah, M. D. Crystal stabilization of α-$FAPbI_3$ perovskite by rapid annealing method in industrial scale. *J. Mater. Res. Technol.* **2021**, *12*, 1924−1930.
(35) Cuzzupè, D. T.; Ünlü, F.; Lê, K.; Bernhardt, R.; Wilhelm, M.; Grosch, M.; Weißingl, R.; Fischer, T.; van Loosdrecht, P. H. M.; Mathur, S. Thermally-induced drift of A-site cations at solid−solid interface in physically paired lead halide perovskites. *Sci. Rep.* **2022**, *12*, No. 10241.
(36) Malevu, T. D.; Ocaya, R. O.; Tshabalala, K. G. Phase transformations of high-purity PbI_2 nanoparticles synthesized from lead-acid accumulator anodes. *Phys. B* **2016**, *496*, 69−73.
(37) Peng, W.; Wang, L.; Murali, B.; Ho, K.-T.; Bera, A.; Cho, N.; Kang, C.-F.; Burlakov, V. M.; Pan, J.; Sinatra, L.; Ma, C.; Xu, W.; Shi, D.; Alarousu, E.; Goriely, A.; He, J.-H.; Mohammed, O. F.; Wu, T.; Bakr, O. M. Solution-Grown Monocrystalline Hybrid Perovskite Films for Hole-Transporter-Free Solar Cells. *Adv. Mater.* **2016**, *28*, 3383−3390.
(38) Fan, P.; Gu, D.; Liang, G.-X.; Luo, J.-T.; Chen, J.-L.; Zheng, Z.-H.; Zhang, D.-P. High-performance perovskite $CH_3NH_3PbI_3$ thin films for solar cells prepared by single-source physical vapour deposition. *Sci. Rep.* **2016**, *6*, No. 29910.
(39) Wang, W.; Wu, Y.; Wang, D.; Zhang, T. Effective Control of the Growth and Photoluminescence Properties of $CsPbBr_3/Cs_4PbBr_6$ Nanocomposites by Solvent Engineering. *ACS Omega* **2019**, *4*, 19641−19646.
(40) Yang, T.; Zheng, Y.-P.; Chou, K.-C.; Hou, X.-M. Tunable fabrication of single-crystalline $CsPbI_3$ nanobelts and their application as photodetectors. *Int. J. Miner. Metall. Mater.* **2021**, *28*, 1030−1037.
(41) Qian, L.; Fu, S.; Li, S.; Miao, R.; Feng, X.; Zhang, W.; Xiao, Z.; Wang, W.; Song, W. High-performance $FAPbBr_3$ perovskite solar cells using dual-function bathocuproine interlayer for surface passivation and energy level alignment. *J. Mater. Sci.:Mater. Electron.* **2022**, *33*, 18028−18038.
(42) Chen, P.; Bai, Y.; Wang, S.; Lyu, M.; Yun, J.-H.; Wang, L. In Situ Growth of 2D Perovskite Capping Layer for Stable and Efficient Solar Cells. *Adv. Funct. Mater.* **2018**, *28*, No. 1706923.
(43) Duan, Z.; Na, G.; Wang, S.; Ning, J.; Xing, B.; Huang, F.; Portniagin, A. S.; Kershaw, S. V.; Zhang, L.; Rogach, A. L. Proton Transfer-Driven Modification of 3D Hybrid Perovskites to Form Oriented 2D Ruddlesden−Popper Phases. *Small Sci.* **2022**, *2*, No. 2100114.
(44) Li, J.; Xiang, P.; Tan, X.; Li, B.; Zhang, K.; Zhu, Y.; Ren, Y.; Chen, X. 3,5-dichlorobenzylamine lead high-performance and stable 2D/3D perovskite solar cells. *J. Mater. Sci.:Mater. Electron.* **2023**, *34*, No. 794.
(45) Park, B.-W.; Kwon, H. W.; Lee, Y.; Lee, D. Y.; Kim, M. G.; Kim, G.; Kim, K.-J.; Kim, Y. K.; Im, J.; Shin, T. J.; Seok, S. I. Stabilization of formamidinium lead triiodide α-phase with isopropylammonium chloride for perovskite solar cells. *Nat. Energy* **2021**, *6*, 419−428.
(46) Zhang, S.; Tang, M.-C.; Nguyen, N. V.; Anthopoulos, T. D.; Hacker, C. A. Wide-Band-Gap Mixed-Halide 3D Perovskites: Electronic Structure and Halide Segregation Investigation. *ACS Appl. Electron. Mater.* **2021**, *3*, 2277−2285.
(47) Liu, Z.-L.; Liu, R.-R.; Mu, Y.-F.; Feng, Y.-X.; Dong, G.-X.; Zhang, M.; Lu, T.-B. In Situ Construction of Lead-Free Perovskite Direct Z-Scheme Heterojunction $Cs_3Bi_2I_9/Bi_2WO_6$ for Efficient Photocatalysis of CO_2 Reduction. *Sol. RRL* **2021**, *5*, No. 2000691.
(48) Xu, C.; Zuo, L.; Hang, P.; Guo, X.; Pan, Y.; Zhou, G.; Chen, T.; Niu, B.; Xu, X.; Hong, Z.; Wang, D.; Zhu, H.; Yu, X.; Yang, D.; Chen, H. Synergistic effects of bithiophene ammonium salt for high-performance perovskite solar cells. *J. Mater. Chem. A* **2022**, *10*, 9971−9980.
(49) Zhao, W.; Liu, D.; Feng, Q. Enhancement of salicylhydroxamic acid adsorption by Pb(II) modified hemimorphite surfaces and its effect on floatability. *Miner. Eng.* **2020**, *152*, No. 106374.
(50) Lu, J.; Jin, R.-N.; Liu, C.; Wang, Y.-F.; Ouyang, X.-K. Magnetic carboxylated cellulose nanocrystals as adsorbent for the removal of Pb(II) from aqueous solution. *Int. J. Biol. Macromol.* **2016**, *93*, 547−556.
(51) Yang, S.; Ke, X.; Chen, Q.; Huang, R.; Wang, W.; Wang, K.; Shu, K.; Tu, C.; Zheng, Z.; Luo, D.; Huang, H.; Zhang, M. In-situ growth behavior of $FAPbBr_3$ on two-dimensional materials for photocatalytic reaction to controllable products. *J. Catal.* **2021**, *402*, 143−153.
(52) Xu, D.; Li, T.; Han, Y.; He, X.; Yang, S.; Che, Y.; Xu, J.; Zou, H.; Guo, X.; Wang, J.; Lei, X.; Liu, Z. Fluorine Functionalized MXene QDs for Near-Record-Efficiency $CsPbI_3$ Solar Cell with High Open-Circuit Voltage. *Adv. Funct. Mater.* **2022**, *32*, No. 2203704.
(53) Han, Q.; Jia, X.; Xu, Y.; Wang, F.; Zhang, Q.; Chen, Y. A. Comparative Study of Structural Contribution to Biocidability via

https://doi.org/10.1021/acsomega.4c11212
ACS Omega 2025, 10, 13327−13338

Immobilization of Fluorinated and Nonfluorinated Quaternary Ammonium Salts on Top Surface. *Langmuir* **2024**, *40*, 23370−23381.
(54) Sun, X.; He, B.; Zhu, J.; Zhu, R.; Chen, H.; Duan, Y.; Tang, Q. Multifunctional brominated graphene oxide boosted charge extraction for high-efficiency and stable all-inorganic $CsPbBr_3$ perovskite solar cells. *Chem. Eng. J.* **2021**, *412*, No. 128727.
(55) Huo, B.; Yang, J.; Bian, Y.; Wu, D.; Feng, J.; Zhou, J.; Huang, Q.; Dong, F.; Tang, X. Amino-mediated anchoring of $FAPbBr_3$ perovskite quantum dots on silica spheres for efficient visible light photocatalytic NO removal. *Chem. Eng. J.* **2021**, *406*, No. 126740.
(56) Zhu, Z.; Hadjiev, V. G.; Rong, Y.; Guo, R.; Cao, B.; Tang, Z.; Qin, F.; Li, Y.; Wang, Y.; Hao, F.; Venkatesan, S.; Li, W.; Baldelli, S.; Guloy, A. M.; Fang, H.; Hu, Y.; Yao, Y.; Wang, Z.; Bao, J. Interaction of Organic Cation with Water Molecule in Perovskite $MAPbI_3$: From Dynamic Orientational Disorder of Hydrogen Bonding. *Chem. Mater.* **2016**, *28*, 7385−7393.
(57) Jancik Prochazkova, A.; Scharber, M. C.; Yumusak, C.; Jančík, J.; MáSilko, J.; Brüggemann, O.; Weiter, M.; Sariciftci, N. S.; Krajcovic, J.; Salinas, Y.; Kovalenko, A. Synthesis conditions influencing formation of $MAPbBr_3$ perovskite nanoparticles prepared by the ligand-assisted precipitation method. *Sci. Rep.* **2020**, *10*, No. 15720.
(58) Pervaiz, S.; Aamir, M.; Wali, Q.; Khan, M. E.; Sattar, M.; Sher, M. Fabrication of aqueous stable $CH_3NH_3PbBr_3$ perovskite: Addressing optoelectronics and fluorescent sensing applications. *Sustainable Chem. Environ.* **2024**, *5*, No. 100059.
(59) Kimura, H. Influence of alternating electric field on electrorheological effect of aqueous dispersions of stevensite. *Appl. Clay Sci.* **2024**, *254*, No. 107393.
(60) Sharma, S.; Kumar, P.; Kumar, M.; Singh, V.; Yocupicio-Gaxiola, R. I.; Siqueiros, J. M.; Herrera, O. R. Investigations on Dielectric, Transport, and Ferroelectric Properties of Ca-Modified $Bi_{0.80}La_{0.20}FeO_3$ Ceramic Synthesized by Solid State Reaction Route. *J. Electron. Mater.* **2023**, *52*, 4312−4320.
(61) Hao, T.; Kawai, A.; Ikazaki, F. Mechanism of the Electrorheological Effect: Evidence from the Conductive, Dielectric, and Surface Characteristics of Water-Free Electrorheological Fluids. *Langmuir* **1998**, *14*, 1256−1262.
(62) Starczewska, A.; Mistewicz, K.; Kozioł, M.; Zubko, M.; Stróż, D.; Dec, J. Interfacial Polarization Phenomena in Compressed Nanowires of SbSI. *Materials* **2022**, *15*, 1543.
(63) Kim, S. G.; Lim, J. Y.; Sung, J. H.; Choi, H. J.; Seo, Y. Emulsion polymerized polyaniline synthesized with dodecylbenzene-sulfonic acid and its electrorheological characteristics: Temperature effect. *Polymer* **2007**, *48*, 6622−6631.
(64) Wen, W.; Huang, X.; Sheng, P. Electrorheological fluids: structures and mechanisms. *Soft Matter* **2008**, *4*, 200−210.
(65) Yoon, C.-M.; Ryu, J.; Yun, J.; Kim, Y. K.; Jang, J. Synthesis of Hierarchical Silica/Titania Hollow Nanoparticles and Their Enhanced Electroresponsive Activity. *ACS Appl. Mater. Interfaces* **2018**, *10*, 6570−6579.
(66) Hoque, M. N. F.; Yang, M.; Li, Z.; Islam, N.; Pan, X.; Zhu, K.; Fan, Z. Polarization and Dielectric Study of Methylammonium Lead Iodide Thin Film to Reveal its Nonferroelectric Nature under Solar Cell Operating Conditions. *ACS Energy Lett.* **2016**, *1*, 142−149.
(67) Wang, X.; Wang, Y.; Gao, W.; Song, L.; Ran, C.; Chen, Y.; Huang, W. Polarization-Sensitive Halide Perovskites for Polarized Luminescence and Detection: Recent Advances and Perspectives. *Adv. Mater.* **2021**, *33*, No. 2003615.
(68) Ramos-Tejada, M. M.; Espin, M. J.; Perea, R.; Delgado, A. V. Electrorheology of suspensions of elongated goethite particles. *J. Non-Newtonian Fluid Mech.* **2009**, *159*, 34−40.
(69) Jiang, J.; Liu, Y.; Shan, L.; Zhang, X.; Meng, Y.; Choi, H. J.; Tian, Y. Shear thinning and shear thickening characteristics in electrorheological fluids. *Smart Mater. Struct.* **2014**, *23*, No. 015003.
(70) Lee, S.; Yoon, C.-M.; Hong, J.-Y.; Jang, J. Enhanced electrorheological performance of a graphene oxide-wrapped silica rod with a high aspect ratio. *J. Mater. Chem. C* **2014**, *2*, 6010−6016.
(71) Sedlacik, M.; Mrlik, M.; Kozakova, Z.; Pavlinek, V.; Kuritka, I. Synthesis and electrorheology of rod-like titanium oxide particles prepared via microwave-assisted molten-salt method. *Colloid Polym. Sci.* **2013**, *291*, 1105−1111.
(72) Hong, J.-Y.; Jang, J. Highly stable, concentrated dispersions of graphene oxide sheets and their electro-responsive characteristics. *Soft Matter* **2012**, *8*, 7348−7350.
(73) Hao, T.; Xu, Z.; Xu, Y. Correlation of the Dielectric Properties of Dispersed Particles with the Electrorheological Effect. *J. Colloid Interface Sci.* **1997**, *190*, 334−340.
(74) Adil, M.; Zaid, H. M.; Chuan, L. K.; Latiff, N. R. A. Effect of Dispersion Stability on Electrorheology of Water-Based ZnO Nanofluids. *Energy Fuels* **2016**, *30*, 6169−6177.
(75) Murugadoss, G.; Thangamuthu, R.; Kumar, S. M. S.; Anandhan, N.; Kumar, M. R.; Rathishkumar, A. Synthesis of ligand-free, large scale with high quality all-inorganic $CsPbI_3$ and $CsPb_2Br_5$ nanocrystals and fabrication of all-inorganic perovskite solar cells. *J. Alloys Compd.* **2019**, *787*, 17−26.
(76) Yoon, C.-M.; Jang, Y.; Noh, J.; Kim, J.; Lee, K.; Jang, J. Enhanced Electrorheological Performance of Mixed Silica Nanomaterial Geometry. *ACS Appl. Mater. Interfaces* **2017**, *9*, 36358−36367.

https://doi.org/10.1021/acsomega.4c11212
ACS Omega 2025, 10, 13327−13338